nature cell biology

Dissecting the molecular architecture of integrin adhesion sites by cryo-electron tomography

Israel Patla[1], Tova Volberg[2], Nadav Elad[1], Vera Hirschfeld-Warneken[3,4], Carsten Grashoff[5], Reinhard Fässler[5], Joachim P. Spatz[3], Benjamin Geiger[2] and Ohad Medalia[1,6]

Focal adhesions are integrin-based multiprotein complexes, several micrometres in diameter, that mechanically link the extracellular matrix with the termini of actin bundles. The molecular diversity of focal adhesions and their role in cell migration and matrix sensing has been extensively studied, but their ultrastructural architecture is still unknown. We present the first three-dimensional structural reconstruction of focal adhesions using cryo-electron tomography. Our analyses reveal that the membrane–cytoskeleton interaction at focal adhesions is mediated through particles located at the cell membrane and attached to actin fibres. The particles have diameters of 25 ± 5 nm, and an average interspacing of approximately 45 nm. Treatment with the Rho-kinase inhibitor Y-27632 induces a rapid decrease in particle diameter, suggesting that they are highly mechanosensitive. Our findings clarify the internal architecture of focal adhesions at molecular resolution, and provide insights into their scaffolding and mechanosensory functions.

Focal adhesions are highly dynamic multiprotein complexes that have scaffolding and signalling roles in the interaction of cells with the extracellular matrix (ECM)[1–3]. The 'adhesome' of focal adhesions is composed of a large variety of actin-associated and adaptor proteins that link F-actin bundles to the membrane[2–9]. The binding of signalling molecules by focal-adhesion proteins can also regulate the structure and dynamics of the cell[6–8]. Together, these constituents of the adhesion complex link the actin cytoskeleton to the extracellular matrix, and transduce a multitude of adhesion signals that affect cell survival, proliferation and differentiation[8,9].

Despite the wealth of information concerning the molecular composition of focal adhesions, the molecular architecture of these sites has not been resolved (for example, see refs 10 and 11). Early electron microscopy studies[1] revealed an electron-dense cytoplasmic layer and cytoskeletal proteins associated with focal adhesions[12–14], but three-dimensional (3D) organization was not characterized.

To gain insights into the molecular architecture of focal adhesions we used a combination of fluorescence microscopy (using cells that express yellow fluorescent protein (YFP)-tagged paxillin, a focal adhesion protein[15,16]) and cryo-electron tomography (which results in minimal disruption of the cell's ultrastructure). Figure 1a shows a fluorescence microscopy image of a REF52 cell expressing YFP–paxillin, cultured on a fibronectin-coated electron-microscope grid[17]. Regions corresponding to focal adhesions were identified and then localized under an electron microscope at low magnification (Fig. 1a, inset), before tilt series of individual focal adhesions were collected (Fig. 1a, arrows). Figure 1b shows a tomographic slice of the focal adhesion marked in Figure 1a.

Actin-containing stress fibres are associated with focal adhesions, and their contractile forces are essential for maintaining the structural integrity of the adhesion site[18–20]. To visualize the architecture of the actin–membrane interface, a 3D surface-rendering of the adhesion site was generated (Fig. 1c). The actin bundle (in brown) was approximately 220 nm thick, thinning gradually to approximately 120 nm towards the end of the bundle. In this reconstruction (Fig. 1c), we counted 532 filaments occupying approximately 25% of the total volume (assuming an 8 nm diameter per single actin filament).

At the core of the focal adhesion, the actin filaments were aligned parallel to the long axis (Fig. 1d), consistent with previous studies[21–23]. In contrast, wide variations in filament orientation were found in peripheral regions of focal adhesions (Fig. 1c). Notably, the distal 200 nm of the focal adhesions appear to be devoid of aligned actin fibres. This finding supports the hypothesis that the proximal and distal ends of focal adhesions display distinct dynamic properties[24–27].

Careful structural assessment of tomographic sections at the stress fibre–membrane interface revealed a large number of small, doughnut-shaped particles with typical diameters of 20–30 nm (Figs 1c and 2a; green). Figure 2a is a re-oriented view of the tomogram presented in Figure 1c, showing that the particles are localized below the actin network at the cell membrane interface. Similar particles were also detected

[1]Department of Life Sciences and the National Institute for Biotechnology in the Negev, Ben Gurion University of the Negev, Be'er-Sheva 84120, Israel. [2]Department of Molecular Cell Biology, Weizmann Institute of Science, Rehovot 76100, Israel. [3]Max-Planck Institute for Metals Research, Department of New Materials and Biosystems, Heisenbergstrasse, 70569 Stuttgart, Germany. [4]University of Heidelberg, Department of Biophysical Chemistry, Stuttgart D-70569, Germany. [5]Max-Planck Institute of Biochemistry, Department of Molecular Medicine, Martinsried D-82152, Germany.
[6]Correspondence should be addressed to O.M. (e-mail: omedalia@bgu.ac.il)

Received 17 February 2010; accepted 05 July 2010; published online 08 August 2010; corrected online 17 August 2010; DOI: 10.1038/ncb2095

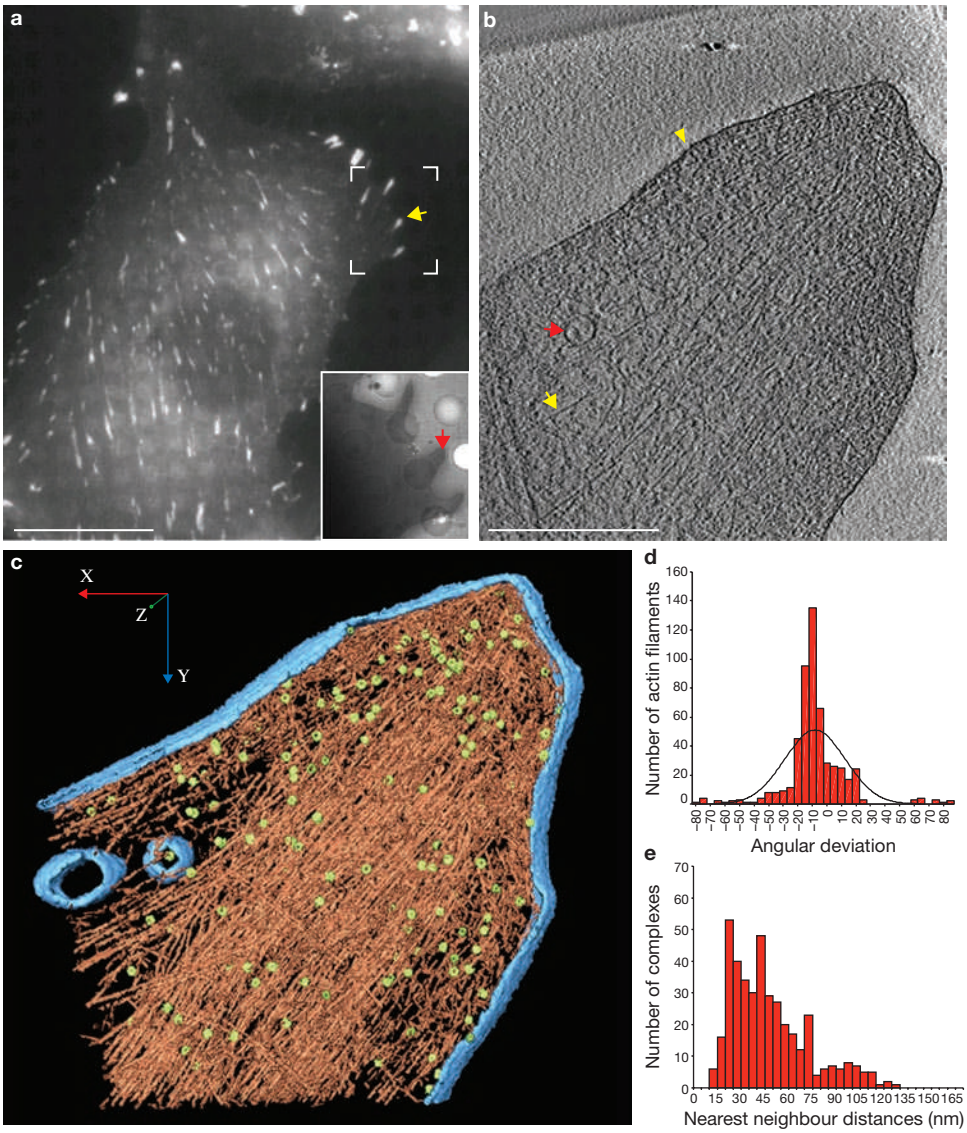

Figure 1 Cryo-electron tomography of integrin-mediated focal adhesions. (**a**) Correlated microscopy, combining fluorescence microscopy at room temperature (using a cell line expressing YFP–paxillin) and cryo-electron tomography. The area indicated by the brackets in **a** was visualized, following vitrification, using low-magnification cryo-electron microscopy (inset) and the individual focal adhesion, indicated by the yellow and red arrows, was subjected to cryo-electron tomography. Scale bar, 20 μm. (**b**) A 10 nm slice through a cryo-tomogram of the focal adhesion indicated in **a** shows aligned actin filaments (yellow arrow), a vesicle (red arrow) and the plasma membrane (yellow arrowhead). Scale bar, 500 nm. (**c**) Surface-rendering view of the focal adhesion site as seen from the direction of the substrate towards the cell. Actin is depicted in brown, membranes in blue and a large number of uniformly-oriented particles located at the interface between the cytoskeletal bundle and the membrane, which are probably adhesion-related particles, are depicted in green. (**d**) A histogram showing the orientation of actin filaments within the focal-adhesion-associated bundle indicates mostly uniform directionality of the actin network. (**e**) A histogram demonstrating the 'nearest neighbour' distance distribution between individual particles. The average centre-to-centre distance calculated between neighbouring particles is 43 ± 20 nm.

outside focal adhesions, but the average density was > 20-fold lower than that found inside (Supplementary Information, Fig. S1). The majority of the particles were oriented with their wider aspects parallel to the actin network (Fig. 1c). We identified 244 such particles in this tomogram (Fig. 1c), equivalent to an average particle density of approximately 170 per μm^2. Similar particle densities were found in each of the reconstructed focal adhesions from REF52 fibroblasts. However, this number should be regarded as a minimal estimate because it is possible that a small percentage of the particles escaped detection, owing to a low local signal-to-noise ratio. The focal-adhesion-associated particles were linked to actin filaments in a variety of configurations (Fig. 2b), suggesting heterogeneity in the attachment of actin filaments to membrane-bound integrin receptors and possibly reflecting variations in the molecular composition of the focal adhesion[28].

Examination of tomographic slices confirmed that the focal-adhesion-associated particles are uniformly oriented, parallel to and positioned 30–70 nm above the carbon ECM support (Fig. 3a, black squares and Supplementary Information, Movie S1). However, the particles were non-uniformly distributed along the adhesion site, and clustered into 'islands' (Fig. 3a), in which the 'nearest neighbour' inter-particle spacing (the mean distance between neighbouring particles' centres of mass) was 43 ± 20 nm (Fig. 1e). Furthermore, the distance between

neighbouring focal-adhesion-associated particles was found to vary with respect to their locations within focal adhesions. Although the inter-particle distances at the focal adhesion periphery were 20–40 nm, their characteristic spacing was 40–70 nm at the centres of focal adhesions (Fig. 1c).

The uniform orientation of the particles relative to the actin-filament network and the plane of the grid prohibited the reconstruction of an isotropically sampled 3D structure[29]. Therefore, the particles were clustered into different structural groups by subjecting them to 2D averaging procedures *in silico,* followed by principle component analysis (PCA) and classification[30]. Twenty-five structural classes of particles were obtained, of which four are presented in Fig. 3b (additional classes are shown in Supplementary Information, Fig. S2a). Figure S2b (Supplementary Information) shows that the structural variations detected are genuine and not attributable to focus differences or their position within the sampled volume. Importantly, the focal-adhesion-associated particles resembled each other in overall morphology, but varied in diameter within a range of 20–30 nm, as well as in the position and apparent number of interacting fibres. These differences may be attributed to variability in the precise composition of the particles throughout the focal adhesion area[7], molecular heterogeneity within focal adhesions[28] or variation in the degree of mechanical force applied to the particles by the associated actin fibres[27,31].

At the centre of the focal adhesions a ratio of approximately 2:1 was found between the numbers of actin filaments and focal-adhesion-associated particles, which is consistent with images shown in Fig. 3b and corroborates the structural classification obtained from the PCA and class average analysis. Notably, the aligned actin bundles appear to interact with the focal-adhesion-associated particles indirectly, through short filaments 200–350 nm in length. These findings suggest that membrane–cytoskeleton interactions and the contractile forces applied to focal adhesions are mediated through the focal-adhesion-associated particles described here.

An essential structural feature of such a model is that the focal-adhesion-associated particles should be positioned between, and mediate, the linkage between the cytoskeletal filaments and the membrane. However, assessment of such direct interactions is difficult. Cryo-electron tomograms provide 3D structural information on focal adhesions at a high spatial resolution of 4–6 nm along the x–y plane (parallel to the cell membrane), but they suffer from a 'missing wedge' in their 3D Fourier space[32] that reduces the resolution along the z-axis, perpendicular to the plane of the membrane. Consequently, the exact position of the substrate-attached plasma membrane cannot be accurately determined (see, for example, Fig. 1). Fortunately, irregularities can often be detected in the electron-microscopy grid that change the angle between the electron beam and the plane of the membrane. Figure S3a, b (Supplementary Information) shows a focal adhesion on such a carbon step, at the edge of a hole in the supported carbon film. Along such a step, the ventral cell membrane assumes a tangential orientation, and can therefore be accurately positioned within the 3D volume. The focal-adhesion-associated particles located on this step appear to interact directly with both the cytoplasmic aspect of the plasma membrane and with the ends of the actin filaments.

A major challenge with the use of cellular cryo-electron tomography at its current resolution (4–6 nm) concerns the accurate identification of macromolecular complexes. Thus, to learn more about the molecular

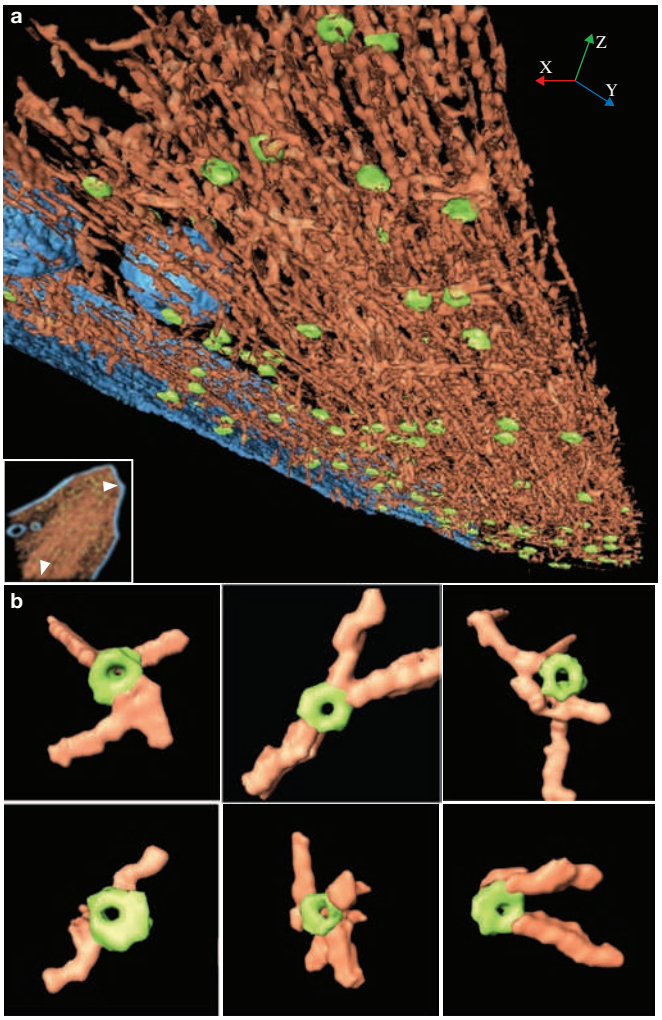

Figure 2 Adhesion-related particles at sites of focal adhesions. (**a**) Surface-rendering view of the same tomogram in Figure 1c, showing a large number of uniformly oriented particles (green) below the cytoskeletal bundle. The orientation of the image, and its exact position relative to Figure 1c, is indicated by the axis marker in both images and by the arrows indicated in the insert. (**b**) Higher-magnification views of the adhesion-related particles depicting their interactions with randomly oriented filaments, which are probably composed of actin.

composition of the focal-adhesion-associated particles, we labelled focal adhesions with immunogold before cryo-electron tomography using 'unroofed cells' from which the dorsal membrane was sheared off, exposing the microfilament system and associated focal adhesions[33]. Following the shearing procedure, focal adhesions were subjected to rapid fixation to retain their native architecture, as previously shown[33]. Such preparation enables the immunolocalization of proteins, followed by their visualization under cryogenic conditions.

Immunolabelling for vinculin was performed by conjugating Protein G to 5 nm colloidal gold particles[34] that were subsequently bound to anti-vinculin antibodies. Vinculin is a canonical component of the adhesion machinery, known to bind to talin and paxillin. As shown in Figure 3c, 5 nm gold clusters were clearly visible within cryo-tomograms of focal adhesions, but rarely found outside of them (Fig. 3d and Supplementary Information, Fig. S3). Views at higher magnification revealed the position of the gold labels in close

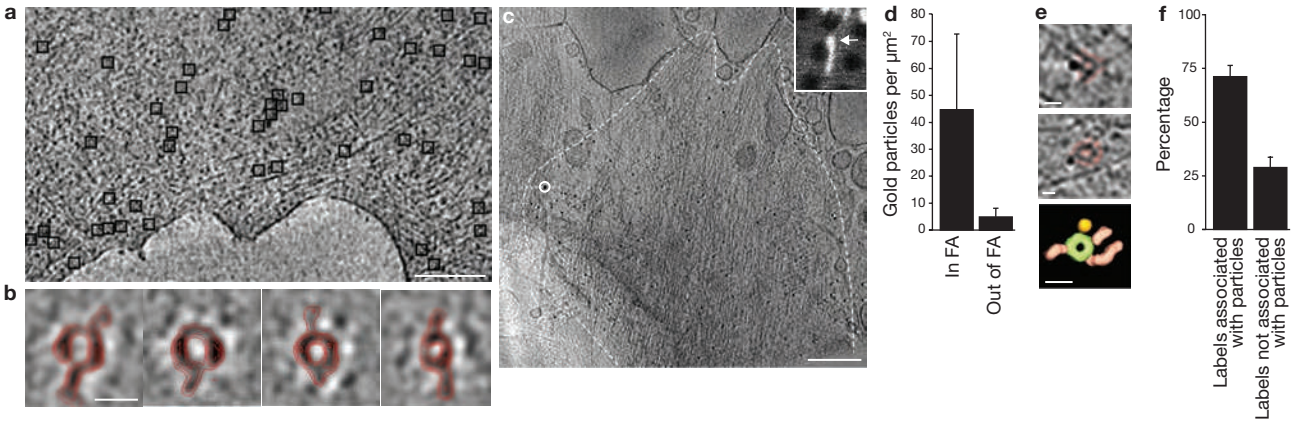

Figure 3 Heterogeneity of adhesion-related particles and vinculin localization. (**a**) An *x*–*y* tomographic slice, 30 nm above the substrate, demonstrating the density of the adhesion-related particles (black boxes). (**b**) Four major structural classes of adhesion particles are shown, with denisty layer lines indicated in red. More classes are shown in Supplementary Information, Figure S2. (**c**) An *x*–*y* tomogram section (80 nm thick) of immunogold-labelled vinculin in a ventral membrane reveals that vinculin is localized within the focal adhesion (a white dashed line defines the focal adhesion area). A 15 nm fiducial gold marker, used to reconstruct the tomogram from the projected images, is indicated by a white circle. A fluorescence microscopy image visualizing YFP–paxillin to determine the focal adhesion is shown in the inset (white arrow). (**d**) Location of the anti-vinculin–gold labels with respect to the focal adhesion (44 ± 28 labels per μm^2 inside focal adhesions, compared with 4.8 ± 3.2 per μm^2 outside of focal adhesions, $n = 511$). (**e**) Zooming in on individual gold labels from **c** indicates the proximity of the vinculin to the adhesion-related complexes. A surface-rendered, adhesion-related complex is shown in the lower panel, together with the 5 nm gold-labelled vinculin (yellow). (**f**) Quantification of the number of labels associated with adhesion-related complexes, compared with those not associated (73% of the labels were found to be associated with the adhesion-related particles, $n = 377$). Error bars represent s.d. Scale bars: **a**, 150 nm; **b**, 21 nm; **c**, 200 nm; **e**, 20 nm.

proximity to the particles (Fig. 3e), suggesting that vinculin is tightly associated with these structures. However, the location of the gold markers was not related to position of the attached fibres. Over 70% of the labels detected within the focal adhesion tomograms were found near definitive particles (Fig. 3f); this number may be larger in intact cells. Further improvements in cryo-electron tomography techniques will be necessary for immunolabelling within intact cells.

Our findings indicate that the focal-adhesion-associated particles are located at key positions between the cellular contractile machinery[4,9,35] and the plasma membrane (Fig. 2a), and thus might be directly subjected to local mechanical forces. We therefore examined the effect of actomyosin relaxation on the distribution and properties of focal-adhesion-associated particles.

REF52 cells were incubated for varying times with contractility inhibitors such as Y-27632, which inhibit Rho-kinase function[36]. Y-27632 affects cellular contractility within a few seconds, as determined by a wrinkling assay using a flexible substrate (data not shown). Figure 4a, b shows that a brief (3 min) treatment of the cells with Y-27632 had almost no effect on the morphology of focal adhesions and the associated actin network, whereas longer treatments with the inhibitors (usually 10 min or more) induced major deterioration (Fig. 4c and see ref. 37 for similar results).

Examination of the focal adhesions in Y-27632-treated cells by cryo-electron tomography indicated that particle morphology underwent considerable change that was already apparent following 3 min of treatment, and persisted after longer incubation (10 or 30 min; Fig. 4d, e). The diameter of the adhesion-related complexes was reduced from approximately 25 nm to 15 nm, although the overall appearance, frequency and the interspacing of these complexes remained similar (Fig. 4d, e). Data shown here are based on experiments conducted with the Rho-kinase inhibitor Y-27632, but similar results were obtained with the kinase inhibitor, H-7, and the actomyosin inhibitor, blebbistatin (data not shown).

Here, we have demonstrated that focal adhesions are layered structures consisting of four major structural domains (schematically depicted in Fig. 5a–d). The outermost domain consists of the plasma membrane, and contains the integrin receptors that anchor the membrane to the corresponding ECM ligands (Fig. 5a). At its cytoplasmic face, the plasma membrane interacts with the doughnut-shaped particles (Fig. 5a, b). Whether this interaction involves direct binding of the integrin receptors to components of the particles remains unclear. Moving upwards and further into the cytoplasm, the focal-adhesion-associated particles interact with short, tangential fibres (Fig. 5a, c) that are associated with the stress fibres (Fig. 5d). The overall area of the entire structure in the *x*–*y* plane varies within a range of several μm^2, and its apparent thickness is approximately 300–350 nm. Thus, superimposing these distinct layers yields a coherent view of the focal adhesion (Fig. 5e, f).

This study provides the first 3D electron microscopy images depicting the molecular architecture of the actin network, and other structural components of focal adhesions. Our analyses indicate that macroscopic focal adhesions are composed of nanoscopic, focal-adhesion-associated particles separated by approximately 43 nm. We previously showed that the assembly of focal adhesions and their associated stress fibres is strictly dependent on similar spacing between the Arg-Gly-Asp (RGD)-ligands present on the adhesive surface[38]. Thus, it seems probable that this spacing is intrinsically regulated by optimal lateral packing of the focal-adhesion-associated particles. We further propose that the functional features of focal adhesions, and their nanoscopic and macroscopic organization, are affected by the particular molecular composition of the adhesion sites; specifically, the lack of a central focal adhesion component. For example, the presence of integrin-linked kinase (ILK) leads concomitantly to increased packing densities and altered dimensions of the focal-adhesion-associated complexes (data not shown).

The formation and dynamics of focal adhesions can be readily explained when the cytoplasmic plaque is composed of well-defined adhesion 'building blocks', nanoscopic in size, rather than being considered as a single, macroscopic protein mesh. It has been extensively documented that application of force to focal adhesions induces their growth[19], and that a typical degree of stress applied to the matrix at focal adhesions is approximately 5.5 nN μm^{-2} (ref. 19). Our findings indicate that the actomyosin contractile forces acting on focal adhesions are mediated through the particles described here, and that the particles are also involved in the mechanosensing activity of focal adhesions[16]. Assuming that the average mechanical stress measured at focal adhesion sites is mediated by 200–300 particles (and applied by approximately 500–600 actin filaments), we suggest that the average tension applied to each particle (by 2–3 actin filaments) is approximately 20 pN, which is in general agreement with the expected force exerted by a few myosin molecules on a single actin fibre[39]. On the basis of ample evidence indicating that forces generated by the actomyosin system are transmitted to the ECM by means of focal adhesions, it is possible that the focal-adhesion-associated particles interact, directly or indirectly, with integrins. Further work will be required to elucidate how focal-adhesion-associated particles interact with integrin receptors.

Our results further indicate that the focal-adhesion-associated particles are mechanosensitive, and their overall morphology is markedly altered on reduction of contractile forces following Rho-kinase inhibition. This effect is observed soon after addition of the inhibitor (approximately 3 min), before reduction in the local levels of paxillin is apparent (< 10%). The mechanism underlying the structural changes in the focal-adhesion-associated particles remains unclear, but could involve loss of components or contraction of the particle, owing to a reduction in the radial pulling forces applied to it. The latter possibility is particularly compelling, as it could provide new insights into the involvement of the particles in the mechanosensitivity of focal adhesions.

As shown in recent years, focal adhesions appear to be molecularly crowded structures, with a multitude of associated protein components[6,8]. Nevertheless, the correlated microscopy approach enabled systematic immuno-electron labelling of unroofed cells, and direct observation of the location of particular molecules relative to the particles or the attached cytoskeleton. This experimental approach has provided information concerning the distribution of vinculin relative to the focal-adhesion-associated particles, and serves as a first step towards extensive proteomic analysis of these structures. The observed structure of focal adhesions shown here is consistent with super-resolution fluorescence studies in which photoactivated light microscopy (PALM) data[40] show that vinculin forms a scattered pattern, similar to the distribution of the particles found in this study. A comprehensive assessment of the detailed molecular composition of these particles will probably require the development of novel biochemical techniques to enable their purification, before detailed proteomic analysis.

The basic structural scaffold of focal adhesions presented here is a major step towards understanding the functional organization of these matrix focal adhesions. The molecular architecture we describe indicates that focal adhesions are modular structures, with overall dimensions that can be regulated by external stimuli (for example, mechanical force) through the assembly or disassembly of 'modules'; namely, the focal-adhesion-associated particles. Furthermore, because of their 'strategic' location between the force-generating cytoskeleton and the matrix-attached membrane, these particles may well function in focal-adhesion-mediated surface mechanosensing, a well-documented phenomenon, whose underlying mechanism is still obscure. Finally, the discovery of the internal structure of focal adhesions may provide new clues to the regulation of their dynamic rearrangement as they grow, on a timescale of minutes or more. Such rearrangement is probably because of recruitment or assembly of particles that constantly exchange components (for example, paxillin or vinculin[27]) on a timescale of seconds. The elucidation of focal adhesion substructures will lead to a mechanistic understanding of these and additional physiological processes mediated through integrin adhesions. □

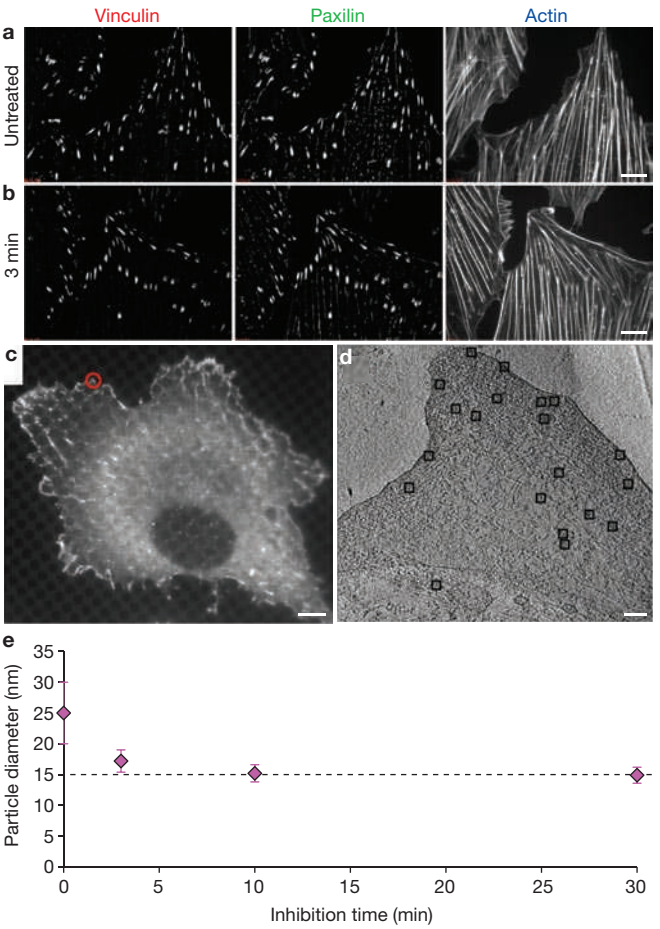

Figure 4 Molecular changes in the adhesion machinery induced by the Rho-kinase inhibitor Y-27632. (**a**–**b**) Cells were left untreated (**a**) or incubated with Y-27632 for 3 min (**b**), and then fixed and triple-immunolabelled for vinculin, paxillin and actin. (**c**–**d**) Correlated microscopy, combining fluorescence microscopy (**c**) and cryo-electron tomography (**d**; from area indicated by red circle in **c**), was used to identify focal adhesion sites after treatment with the Rho-kinase inhibitor for 30 min. The *x*–*y* tomographic slice shown is 30 nm above the substrate and indicates that the frequency of the adhesion-related particles (black boxes) was not strongly affected. (**e**) The dimensions of the adhesion-related particles on incubation with the Rho-kinase inhibitor, Y-27632. This effect was already apparent following 3 min of Y-27632 treatment, and persisted on further incubation with Y-27632 for 10 or 30 min. Scale bars: **a**, **b**, 10 μm; **c**, 10 μm; **d**, 60 nm.

METHODS

Methods and any associated references are available in the online version of the paper at http://www.nature.com/naturecellbiology/

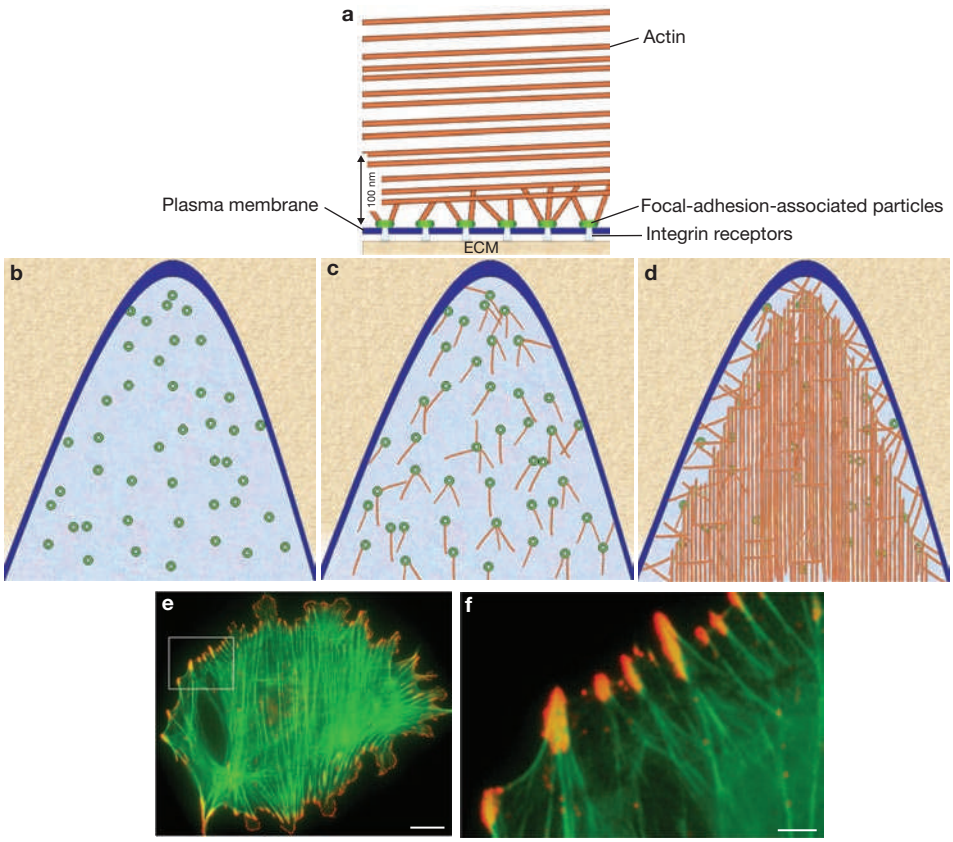

Figure 5 Architecture of focal adhesions at nanoscale resolution. Model of a focal adhesion's ultrastructure, showing (**a**) an *x–z* view and (**b**–**d**) three *x–y* views at increasing distance from the extracellular matrix. (**a**) An actin bundle is shown (approximately 200 nm thick), connected to the membrane-bound focal-adhesion-associated particles through short actin filaments. (**b**) Above the matrix-attached plasma membrane are the focal-adhesion-associated particles. (**c**) Inside the focal adhesion, particles are shown interacting with short filaments. (**d**) The well-structured, bundled actin network is involved in applying force to the adhesion site. Nevertheless, the unbundled actin network is seen in the outermost layer of the focal adhesion. (**e**–**f**) Focal adhesions and associated actin filaments are shown by fluorescence microscopy in **e** and in greater detail in **f**, depicting the actin network (green) and focal adhesions stained for phosphotyrosine (red). Scale bars: **e**, 10 μm; **f**, 2 μm.

Note: Supplementary Information is available on the Nature Cell Biology website

ACKNOWLEDGEMENTS

This study was supported by a grant from the German-Israeli Cooperation Project (DIP H.2.2) to O. M., R. F., J. S. and B. G., an NIGMS grant from the National Institutes of Health Cell Migration Consortium (Grant No. U54 GM64346) to B. G. and an ERC Starting Grant to O. M. The authors express gratitude to B. Morgenstern for help in editing the manuscript. B. G. holds the Erwin Neter Professorial Chair in Cell and Tumor Biology.

AUTHOR CONTRIBUTIONS

I. P., N. E., T. V., C. G. and V. H. W. performed experimental work and analysed the data. B. G., J. S., R. F. and O. M. designed the experiments, analysed the data and prepared the manuscript.

COMPETING FINANCIAL INTERESTS

The authors declare no competing financial interests.

Published online at http://www.nature.com/naturecellbiology
Reprints and permissions information is available online at http://npg.nature.com/reprintsandpermissions/

1. Abercrombie, M. & Dunn, G. A. Adhesions of fibroblasts to substratum during contact inhibition observed by interference reflection microscopy. *Exp. Cell. Res.* **92,** 57–62 (1975).
2. Wiesner, S., Lange, A. & Fässler, R. Local call: from integrins to actin assembly. *Trends Cell Biol.* **16,** 327–329 (2006).
3. Ginsberg, M., Pierschbacher, M. D., Ruoslahti, E., Marguerie, G. & Plow, E. Inhibition of fibronectin binding to platelets by proteolytic fragments and synthetic peptides which support fibroblast adhesion. *J. Biol. Chem.* **260,** 3931–3936 (1985).
4. Burridge, K., Fath, K., Kelly, T., Nuckolls, G. & Turner, C. Focal adhesions: transmembrane junctions between the extracellular matrix and the cytoskeleton. *Annu. Rev. Cell Biol.* **4,** 487–525 (1988).
5. Campbell, I. D. Studies of focal adhesion assembly. *Biochem. Soc. Trans.* **36,** 263–266 (2008).
6. Zamir, E. & Geiger, B. Molecular complexity and dynamics of cell–matrix adhesions. *J. Cell Sci.* **114,** 3583–3590 (2001).
7. Zaidel-Bar, R., Itzkovitz, S., Ma'ayan, A., Iyengar, R. & Geiger, B. Functional atlas of the integrin adhesome. *Nat. Cell Biol.* **9,** 858–867 (2007).
8. Legate, K. R., Wickstrom, S. A. & Fässler, R. Genetic and cell biological analysis of integrin outside–in signaling. *Genes Dev.* **23,** 397–418 (2009).
9. Geiger, B., Spatz, J. P. & Bershadsky, A. D. Environmental sensing through focal adhesions. *Nat. Rev. Mol. Cell Biol.* **10,** 21–33 (2009).
10. Winograd-Katz, S. E., Itzkovitz, S., Kam, Z. & Geiger, B. Multiparametric analysis of focal adhesion formation by RNAi-mediated gene knockdown. *J. Cell Biol.* **186,** 423–436 (2009).
11. Delon, I. & Brown, N. H. Integrins and the actin cytoskeleton. *Curr. Opin. Cell Biol.* **19,** 43–50 (2007).
12. Feltkamp, C. A., Pijnenburg, M. A. & Roos, E. Organization of talin and vinculin in adhesion plaques of wet-cleaved chicken embryo fibroblasts. *J. Cell Sci.* **100,** 579–587 (1991).
13. Nicol, A. *et al.* Labeling of structural elements at the ventral plasma membrane of fibroblasts with the immunogold technique. *J. Histochem. Cytochem.* **35,** 499–506 (1987).
14. Rinnerthaler, G., Geiger, B. & Small, J. V. Contact formation during fibroblast locomotion: involvement of membrane ruffles and microtubules. *J. Cell Biol.* **106,** 747–760 (1988).
15. Turner, C. E. & Miller, J. T. Primary sequence of paxillin contains putative SH2 and SH3 domain binding motifs and multiple LIM domains: identification of a vinculin and pp125Fak-binding region. *J. Cell Sci.* **107,** 1583–1591 (1994).
16. Salgia, R. *et al.* Molecular cloning of human paxillin, a focal adhesion protein phosphorylated by P210BCR/ABL. *J. Biol. Chem.* **270,** 5039–5047 (1995).
17. Medalia, O. *et al.* Macromolecular architecture in eukaryotic cells visualized by cryo-electron tomography. *Science* **298,** 1209–1213 (2002).

18. Vogel, V. & Sheetz, M. Local force and geometry sensing regulate cell functions. *Nat. Rev. Mol. Cell Biol.* **7,** 265–275 (2006).
19. Riveline, D. *et al.* Focal contacts as mechanosensors: externally applied local mechanical force induces growth of focal contacts by an mDia1-dependent and ROCK-independent mechanism. *J. Cell Biol.* **153,** 1175–1186 (2001).
20. Chrzanowska-Wodnicka, M. & Burridge, K. Rho-stimulated contractility drives the formation of stress fibers and focal adhesions. *J. Cell Biol.* **133,** 1403–1415 (1996).
21. Lo, S. H. Focal adhesions: what's new inside. *Dev. Biol.* **294,** 280–291 (2006).
22. Petit, V. & Thiery, J. P. Focal adhesions: structure and dynamics. *Biol. Cell* **92,** 477–494 (2000).
23. Singer, I. I. The fibronexus: a transmembrane association of fibronectin-containing fibers and bundles of 5 nm microfilaments in hamster and human fibroblasts. *Cell* **16,** 675–685 (1979).
24. Waterman-Storer, C. M., Salmon, W. C. & Salmon, E. D. Feedback interactions between cell–cell adherens junctions and cytoskeletal dynamics in newt lung epithelial cells. *Mol. Biol. Cell* **11,** 2471–2483 (2000).
25. Nicolas, A., Besser, A. & Safran, S. A. Dynamics of cellular focal adhesions on deformable substrates: consequences for cell force microscopy. *Biophys. J.* **95,** 527–539 (2008).
26. Beningo, K. A. & Wang, Y. L. Flexible substrata for the detection of cellular traction forces. *Trends Cell Biol.* **12,** 79–84 (2002).
27. Wolfenson, H. *et al.* A role for the juxtamembrane cytoplasm in the molecular dynamics of focal adhesions. *PLoS One* **4,** e4304 (2009).
28. Zamir, E., Geiger, B. & Kam, Z. Quantitative multicolor compositional imaging resolves molecular domains in cell–matrix adhesions. *PLoS ONE* **3,** e1901 (2008).
29. Frank, J. *Electron Tomography* (ed. Frank, J.) 1–13 (Plenum, 1992).
30. van Heel, M. Multivariate statistical classification of noisy images (randomly oriented biological macromolecules). *Ultramicroscopy* **13,** 165–183 (1984).
31. Wolfenson, H., Henis, Y. I., Geiger, B. & Bershadsky, A. D. The heel and toe of the cell's foot: a multifaceted approach for understanding the structure and dynamics of focal adhesions. *Cell Motil. Cytoskeleton* **66,** 1017–1029 (2009).
32. Jimenez, J., Santisteban, A., Carazo, J. M. & Carrascosa, J. L. Computer graphic display method for visualizing three-dimensional biological structures. *Science* **232,** 1113–1115 (1986).
33. Avnur, Z. & Geiger, B. Substrate-attached membranes of cultured cells isolation and characterization of ventral cell membranes and the associated cytoskeleton. *J. Mol. Biol.* **153,** 361–379 (1981).
34. Slot, J. W. & Geuze, H. J. A new method of preparing gold probes for multiple-labeling cytochemistry. *Eur. J. Cell Biol.* **38,** 87–93 (1985).
35. Schwartz, M. A. & DeSimone, D. W. Cell adhesion receptors in mechanotransduction. *Curr. Opin. Cell Biol.* **20,** 551–556 (2008).
36. Narumiya, S., Ishizaki, T. & Uehata, M. Use and properties of ROCK-specific inhibitor Y-27632. *Methods Enzymol.* **325,** 273–284 (2000).
37. Katoh, K., Kano, Y. & Ookawara, S. Rho-kinase dependent organization of stress fibers and focal adhesions in cultured fibroblasts. *Genes Cells* **12,** 623–638 (2007).
38. Cavalcanti-Adam, E. A. *et al.* Cell spreading and focal adhesion dynamics are regulated by spacing of integrin ligands. *Biophys. J.* **92,** 2964–2974 (2007).
39. Finer, J. T., Simmons, R. M. & Spudich, J. A. Single myosin molecule mechanics: piconewton forces and nanometre steps. *Nature* **368,** 113–119 (1994).
40. Betzig, E. *et al.* Imaging intracellular fluorescent proteins at nanometer resolution. *Science* **313,** 1642–1645 (2006).

DOI: 10.1038/ncb2095

METHODS

Cell cultures. REF52 cells expressing YFP–paxillin were cultured in Dulbecco's Modified Eagle's Medium (DMEM; Biological Industries) supplemented with 10% (v/v) fetal calf serum (FCS, Biological Industries), 5 ml of L-glutamine (0.2 M, Biological Industries) and 5 ml of penicillin–streptomycin–nystatin (Biological Industries), at 37 °C and 5% CO_2.

Cryo-electron tomography. Carbon-coated 200-mesh gold grids (Quantifoil) were rinsed in PBS (Biological Industries) and overlaid on a drop of 50 μg ml^{-1} fibronectin (Calbiochem) for 45 min. Cells were applied to grids in concentrations of 100 cells per grid, and then cultured for 24 h. A 5 μl drop of bovine serum albumin (BSA)-coated 15 nm gold colloids in PBS was added to each grid, before plunging them into liquid nitrogen-cooled ethane, as previously described[41]. Specimens were then transferred into a 300 FEG Polara microscope (FEI) equipped with a Gatan post-column GIF 2002 energy filter. Tilt series were collected, covering an angular range of –60° to 66°, sampled in 2° tilt increments, and at a 14 μm or 9 μm underfocus for gold-labelled ventral membranes. Pixel size was 0.82 nm at the specimen level.

Fluorescence imaging and correlative microscopy. Fluorescence microscopy was conducted under cryogenic conditions, as previously described[42], or before vitrification of the sample using chemical fixation. In both cases, the resulting cryo-tomograms were indistinguishable.

REF52 cells expressing YFP–paxillin were cultured on electron-microscopy grids and freeze-plunged or incubated for 30 min in PBS containing 3% (v/v) paraformaldehyde. Following fluorescence microscopy imaging, grids were washed with PBS and instantly plunged into liquid-nitrogen-cooled ethane.

Focal adhesions were identified with fluorescently labelled paxillin and indexed according to their positions on the grid. The coordinates of each focal adhesion site were recorded and identified under the electron microscope. Fluorescence microscopy images were acquired with a DeltaVision system (Applied Precision) equipped with a CoolSnap HQ camera (Photometric) operated by SoftWorx and Resolve3D software (Applied Precision), using an Olympus PlanApoN ×60, 1.42 NA objective on an Olympus IX70 inverted microscope.

Synthesis of colloidal gold–Protein G conjugates. Recombinant Protein G (2 μl; Invitrogen) was added to 1 ml of freshly prepared 5 nm gold colloid solution[43]. The amount of protein needed for stabilizing the colloidal gold solution was determined by Zygmondy's test, as previously described[43]. After 5 min, BSA was added to a final concentration of 0.2%. The solution was centrifuged at 210,000*g* for 30 min at 4 °C, and the pellet was diluted in PBS containing BSA (to a final concentration of 0.2%) to an A_{520} of 0.5.

Cryo-electron tomography of ventral membrane preparations and immunolabelling. Shearing of the dorsal membrane ('unroofing') was performed as previously described[44]. In brief, REF52 cells expressing YFP–paxillin grown on electron-microscopy grids were washed with PBS and sprayed with buffer (30 mM Pipes, 25 mM Hepes, 2mM $MgSO_2$ and 10 mM EGTA, adjusted to pH 6.6). Cell shearing was monitored by phase contrast light microscopy. Cells were then fixed in 3% (v/v) paraformaldehyde, and focal adhesions were indexed. Grids were incubated for 45 min with rabbit anti-vinculin (1:100; Sigma, V4139), washed three times with PBS for 5 min each, followed by 15 min blocking with 5% (v/v) BSA in PBS. The grids were then incubated with Protein G–5 nm colloidal gold conjugates for 45 min, before extensive washing with PBS. Grids were plunge-frozen and transferred into the electron microscope under cryogenic conditions for tomographic data acquisition. As a control, the procedure was repeated with no antibody incubation. The position of 5 nm gold clusters was recorded and every gold particle at a distance < 10 nm from the adhesion-related particles was considered to be localized to the particles, as we assumed the effective distance of an immunoglobulin G (IgG) bound to 5 nm gold is a maximum of 10 nm.

Inhibition of Rho-kinase by Y-27632. The Rho-kinase inhibitor Y-27632 (Calbiochem, 6880000) was added at a concentration of 10 μM to cultured REF52 cells expressing YFP–paxillin, 16 h after plating them on glass coverslips. Cells were fixed chemically after 3, 10 or 30 min of incubation and then subjected to correlative fluorescence microscopy, followed by cryo-tomography, as described above.

Image processing. Image processing was carried out using Prism software for Linux (http://msg.ucsf.edu/IVE/index.html). Projection images (2048 × 2048) were aligned to a common origin, using 15-nm-sized fiducial gold markers, and reconstructed by means of weighted back-projection, as implemented by the TOM toolbox software package[45]. All tomograms were reconstructed with a binning factor, to yield a 1.64 nm voxel size.

For visualization purposes, the reconstructed volumes were processed by an anisotropic de-noising algorithm[46]. Individual adhesion complexes were identified and extracted *in silico*. Two-dimensional images of these elements were calculated by projecting the volumes (32 × 32 × 11 voxels) along the *z* axis, using the electron-microscopy software package[47]. We selected the six best tomograms from each experiment to analyse the particles: this typically yielded approximately 1,500 particles. The stack of particles was then masked and normalized before PCA, followed by K-means classification (SPIDER). The most detailed class averages were chosen to be the first references for a multi-reference alignment of the dataset. This strategy was iterated for five rounds, until no major changes occurred in the classes, and in the alignment of single images.

Surface-rendered visualizations were constructed using the surface-rendering option in AMIRA 4.1 software (Mercury). A 3D mask for actin filaments was prepared manually (filaments were defined by a characteristic diameter of approximately 10 nm, and persistence of > 20 nm), and a 3D threshold was applied to the masked tomogram, preserving the original densities. The focal-adhesion-associated particles were segmented in a similar fashion, using a 30 nm spherical filter. To assist visualization, the filaments, particles and membranes were subjectively coloured brown, green and blue, respectively.

41. Dubochet, J. *et al.* Cryo-electron microscopy of vitrified specimens. *Q. Rev. Biophys.* **21,** 129–228 (1988).
42. Sartori, A. *et al.* Correlative microscopy: bridging the gap between fluorescence light microscopy and cryo-electron tomography. *J. Struct. Biol.* **160,** 135–145 (2007).
43. Slot, J. W. & Geuze, H. J. A new method of preparing gold probes for multiple-labeling cytochemistry. *Eur. J. Cell Biol.* **38,** 87–93 (1985).
44. Avnur, Z. & Geiger, B. Substrate-attached membranes of cultured cells isolation and characterization of ventral cell membranes and the associated cytoskeleton. *J. Mol. Biol.* **153,** 361–379 (1981).
45. Nickell, S. *et al.* TOM software toolbox: acquisition and analysis for electron tomography. *J. Struct. Biol.* **149,** 227–234 (2005).
46. Frangakis, A. S. & Hegerl, R. Noise reduction in electron tomographic reconstructions using nonlinear anisotropic diffusion. *J. Struct. Biol.* **135,** 239–250 (2001).
47. Hegerl, R. The EM Program Package: a platform for image processing in biological electron microscopy. *J. Struct. Biol.* **116,** 30–34 (1996).

CORRIGENDUM

Dissecting the molecular architecture of integrin adhesion sites by cryo-electron tomography

Israel Patla, Tova Volberg, Nadav Elad, Vera Hirschfeld-Warneken, Carsten Grashoff, Reinhard Fässler, Joachim P. Spatz, Benjamin Geiger and Ohad Medalia

Nat. Cell Biol. **12,** DOI: 10.1038/ncb2095; published online 8 August 2010; corrected after print, 17 August 2010

In the version of this letter initially published online, Vera Hirschfeld-Warneken was incorrectly spelled in the author list. This error has been corrected in both the HTML and PDF versions of the letter.

nature cell biology

DOI: 10.1038/ncb2095

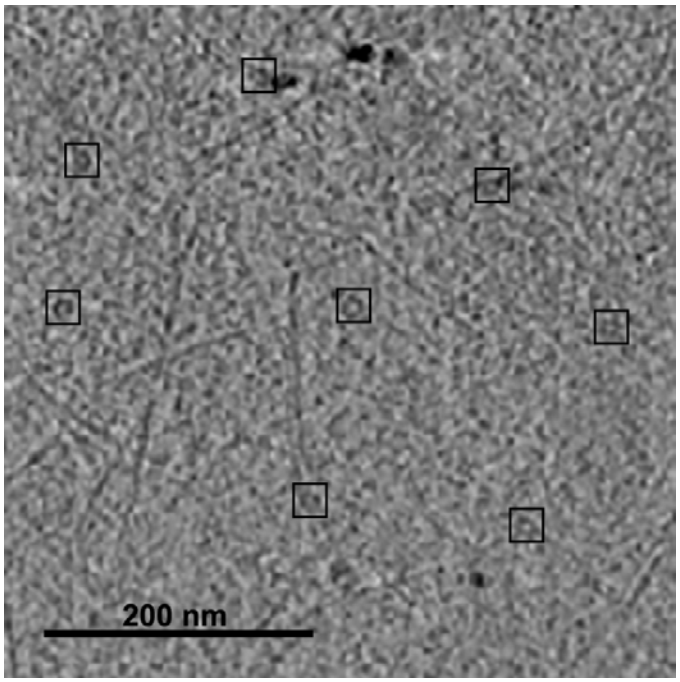

Figure S1 Adhesion-related particles at non-adhesive sites. An x-y tomographic slice, taken from the bottom of a cell, in a non-adhesive region, indicates the low density of adhesion-related particles.

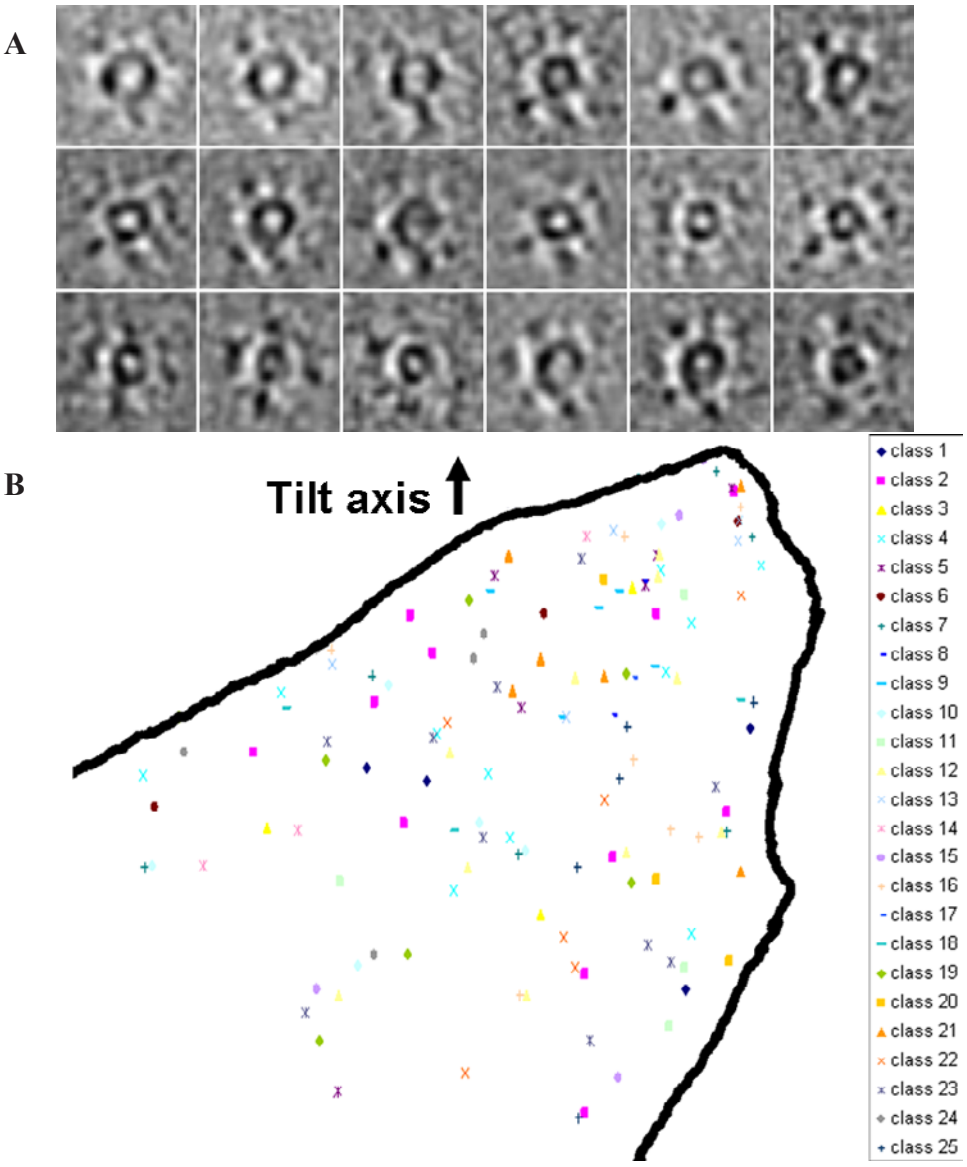

Figure S2 Class averages of the adhesion related-particles. (**A**). Of a total of 25 classes of adhesion-related particles in REF52 cells, 18 class averages are shown (see Materials and Methods). These classes were converged by iterative alignment and classification procedures. When adhesion-related particles were separated into a larger number of classes (e.g., 50 or 100), novel features were not observed, while their separation into a smaller number of classes (e.g., 10) resulted in the fading of particle features, indicating the existence of about 25 classes. It is noteworthy that the additional 7 classes not shown exhibit a small number of particles, resulting in a lower S/N ratio. (**B**) The distribution of the classes is independent of the relative position of the tilt axis, indicating the inherent structural differences among the classes.

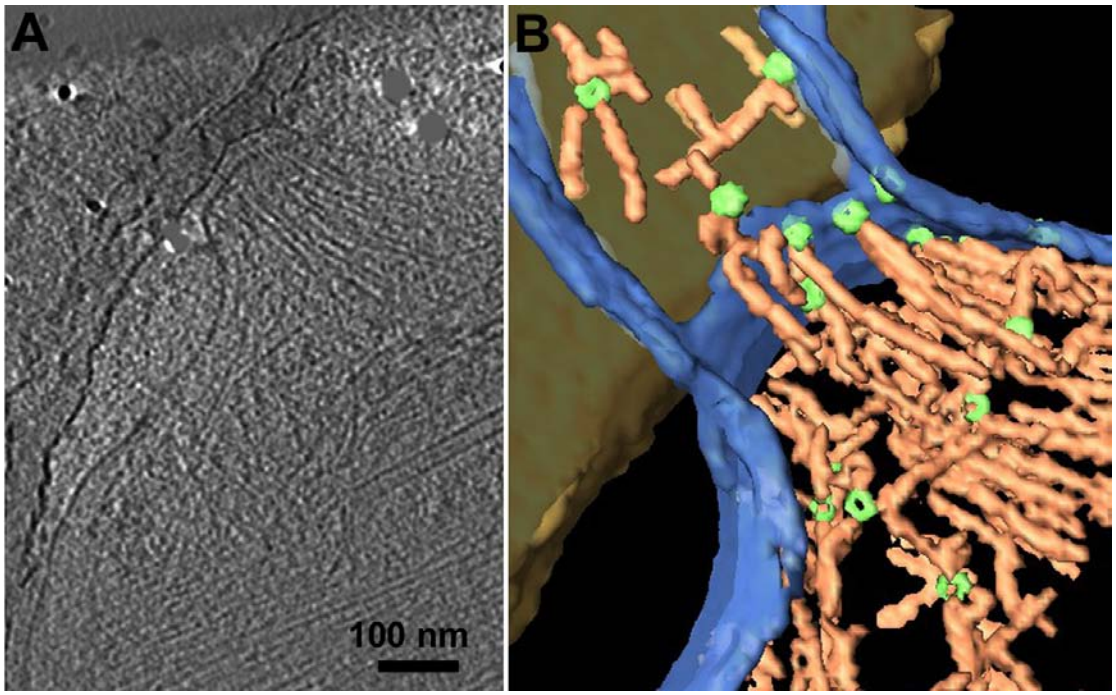

Figure S3 Adhesion-related particles are attached to the cytoplasmic aspect of the plasma membrane. (**A**) A 7-nm x-y slice through a cell that spread over a step in the carbon substrate, enabling accurate tangential visualization of the particle-plasma membrane interface. To obtain better contrast, some fiducial gold markers were masked. (**B**) Surface rendering view of the same area, displaying part of the actin network within a 480 nm × 480 nm area from the reconstructed volume shown in (**A**), indicates the close interactions of the adhesion-associated particles (light green) with the cytoplasmic aspect of the plasma membrane, bridging the cytoskeletal filaments (reddish brown) and the plasma membrane (blue).

Movie S1 Cryo-ET anlysis of focal adhesion